

Air temperature optima of vegetation productivity across global biomes

Mengtian Huang¹, Shilong Piao^{1,2,3*}, Philippe Ciais⁴, Josep Peñuelas^{5,6}, Xuhui Wang¹, Trevor F. Keenan^{7,8}, Shushi Peng⁹, Joseph A. Berry⁹, Kai Wang¹, Jiafu Mao¹⁰, Ramdane Alkama¹¹, Alessandro Cescatti¹¹, Matthias Cuntz¹², Hannes De Deurwaerder¹³, Mengdi Gao¹, Yue He¹, Yongwen Liu¹, Yiqi Luo¹⁴, Ranga B. Myneni¹⁵, Shuli Niu¹⁶, Xiaoying Shi¹⁰, Wenping Yuan¹⁷, Hans Verbeeck¹³, Tao Wang^{2,3}, Jin Wu^{18,19} and Ivan A. Janssens²⁰

The global distribution of the optimum air temperature for ecosystem-level gross primary productivity ($T_{\text{opt}}^{\text{eco}}$) is poorly understood, despite its importance for ecosystem carbon uptake under future warming. We provide empirical evidence for the existence of such an optimum, using measurements of in situ eddy covariance and satellite-derived proxies, and report its global distribution. $T_{\text{opt}}^{\text{eco}}$ is consistently lower than the physiological optimum temperature of leaf-level photosynthetic capacity, which typically exceeds 30 °C. The global average $T_{\text{opt}}^{\text{eco}}$ is estimated to be 23 ± 6 °C, with warmer regions having higher $T_{\text{opt}}^{\text{eco}}$ values than colder regions. In tropical forests in particular, $T_{\text{opt}}^{\text{eco}}$ is close to growing-season air temperature and is projected to fall below it under all scenarios of future climate, suggesting a limited safe operating space for these ecosystems under future warming.

Understanding how photosynthesis responds to warming has been a focus in plant research in recent decades, and most of the existing knowledge comes from leaf-scale measurements^{1–4}. Most leaf-scale temperature response curves show that photosynthetic capacity increases with temperature up to an optimum temperature ($T_{\text{opt}}^{\text{leaf}}$), which typically occurs in the 30–40 °C temperature range^{5,6}. Above this optimum temperature, foliar photosynthetic capacity sharply declines as electron-transport and Rubisco enzymatic capacities become impaired⁷. Field et al.⁸ suggested that ecosystem-scale optimum temperature $T_{\text{opt}}^{\text{eco}}$ may differ from $T_{\text{opt}}^{\text{leaf}}$. At the ecosystem scale, elevated air temperatures do limit canopy photosynthesis by processes other than leaf carboxylation rates. For instance, elevated air temperatures may accelerate leaf ageing and increase leaf thickness (phenology; for example, ref. ⁹) and control stomatal closure because a higher temperature usually comes with a higher vapour pressure deficit (VPD)¹⁰. In a more extreme case, warming-induced water stress could suppress canopy photosynthesis through partial hydraulic failure (hydraulics) by cavitation (for example, ref. ¹¹).

Empirical leaf-scale photosynthesis–temperature relationships¹² have been directly incorporated into global ecosystem models, with variants to account for acclimation, that is, a temporal adjustment of optimum photosynthetic temperature to air temperature during growth^{5,13,14}. This direct scaling of temperature responses from

leaves to ecosystems partly determines model projections of gross primary productivity (GPP) and CO₂ uptake by terrestrial ecosystems in climatic scenarios. Verifying the existence of $T_{\text{opt}}^{\text{eco}}$ in real-world ecosystems, defining its spatial distribution across and within biomes, and understanding the relationships between $T_{\text{opt}}^{\text{eco}}$, prevailing air temperature and $T_{\text{opt}}^{\text{leaf}}$ are important for evaluating models and understanding the impacts of various climatic warming targets on ecosystem productivity.

In this study, we formulate and test the following hypotheses: (1) $T_{\text{opt}}^{\text{eco}}$ is higher for biomes when air temperature during growth is warmer, (2) $T_{\text{opt}}^{\text{eco}}$ is lower than $T_{\text{opt}}^{\text{leaf}}$ for any given ecosystem because the limitations mentioned earlier of stomatal conductance and phenology emerge before temperature begins to impair foliar photosynthetic capacity, and (3) tropical forests already operate near a high $T_{\text{opt}}^{\text{eco}}$ above which canopy photosynthesis may decrease with even moderate air temperature warming^{15,16}. Here, we defined $T_{\text{opt}}^{\text{eco}}$ as the daytime air temperature at which GPP is highest over a period of several years, and thus $T_{\text{opt}}^{\text{eco}}$ can be empirically determined from productivity observations and proxies (see Methods).

Results and discussion

We first applied this approach on time series of daily GPP derived from CO₂ flux measurements at 153 globally distributed eddy covariance sites and found that a robust estimate of $T_{\text{opt}}^{\text{eco}}$ could be derived

¹Sino-French Institute for Earth System Science, Peking University, Beijing, China. ²Key Laboratory of Alpine Ecology and Biodiversity, Chinese Academy of Sciences, Beijing, China. ³Center for Excellence in Tibetan Earth Science, Chinese Academy of Sciences, Beijing, China. ⁴Laboratoire des Sciences du Climat et de l'Environnement, Gif-sur-Yvette, France. ⁵Centre for Research on Ecology and Forestry Applications, Barcelona, Spain. ⁶CSIC, Global Ecology Unit CREAM-CSIC-UAB, Barcelona, Spain. ⁷Lawrence Berkeley National Laboratory, Berkeley, CA, USA. ⁸Department of Environmental Science Policy and Management, UC Berkeley, Berkeley, CA, USA. ⁹Department of Global Ecology, Carnegie Institution for Science, Stanford, CA, USA. ¹⁰Climate Change Science Institute and Environmental Sciences Division, Oak Ridge National Laboratory, Oak Ridge, TN, USA. ¹¹European Commission, Joint Research Centre (JRC), Ispra, Italy. ¹²Université de Lorraine, INRA, AgroParisTech, UMR Silva, Nancy, France. ¹³CAVElab Computational and Applied Vegetation Ecology, Ghent University, Ghent, Belgium. ¹⁴Department of Biological Sciences, Northern Arizona University, Flagstaff, AZ, USA. ¹⁵Department of Earth and Environment, Boston University, Boston, MA, USA. ¹⁶Key Laboratory of Ecosystem Network Observation and Modeling, Chinese Academy of Sciences, Beijing, China. ¹⁷School of Atmospheric Sciences, Sun Yat-Sen University, Guangzhou, China. ¹⁸Environmental and Climate Sciences Department, Brookhaven National Laboratory, Upton, NY, USA. ¹⁹School of Biological Sciences, University of Hong Kong, Pokfulam, Hong Kong. ²⁰Centre of Excellence – Plants and Vegetation Ecology, University of Antwerp, Wilrijk, Belgium. *e-mail: slpiao@pku.edu.cn

at 125 out of 153 sites (see Methods). $T_{\text{opt}}^{\text{eco}}$ values derived from the FLUXNET data range from 8.2 °C to 35.8 °C (Fig. 1a, Supplementary Table 1). Tropical sites have higher $T_{\text{opt}}^{\text{eco}}$ values than temperate and boreal sites (Supplementary Fig. 1), implying a dependency of $T_{\text{opt}}^{\text{eco}}$ on background climate. The FLUXNET multi-site analysis further indicates that $T_{\text{opt}}^{\text{eco}}$ values across sites are positively correlated with daily maximum air temperature averaged over the growing season ($T_{\text{max gs}}^{\text{air}}$, see calculation in Methods) ($R=0.46$, $P<0.01$, t -test), with a spatial linear regression slope of 0.61 °C per °C across sites (Fig. 1a). Overall, these results confirm our first hypothesis, which stated that higher $T_{\text{opt}}^{\text{eco}}$ values occur when higher growth temperatures prevail, in support of findings in refs. 17,18.

Since eddy covariance measurements do not have a continuous spatial coverage, we also used satellite observations known to be highly correlated with photosynthetic activity¹⁹, that is, GPP proxies. The first proxy used is NIR_v , the product of total scene NIR reflectance (NIR_r) by the NDVI. NIR_v was proven to have a high temporal correlation with GPP at flux-tower sites¹⁹. Satellite observations of NIR_r and NDVI from the terra MODIS were used to calculate NIR_v between 2001 and 2013 (see Methods). NIR_v -derived $T_{\text{opt}}^{\text{eco}}$ is comparable to that estimated from eddy covariance flux-tower measurements (Fig. 1b), which gives support to using the NIR_v proxy for a global mapping of $T_{\text{opt}}^{\text{eco}}$. The average $T_{\text{opt}}^{\text{eco}}$ over the global vegetated areas is estimated to be 23 ± 6 °C (mean ± 1 s.d.) with large spatial gradients in latitude. As shown in Fig. 1c, maximum values close to 30 °C mainly appear over tropical forests, savannas and drylands and minimum values near 10 °C prevail at high latitudes and in mountainous regions (Fig. 1c). This spatial pattern of $T_{\text{opt}}^{\text{eco}}$ is robust to the choice of a particular climate-forcing dataset or to the method used to estimate $T_{\text{opt}}^{\text{eco}}$ (Supplementary Fig. 2, see also Methods). Similar results are also found for other GPP proxies (vegetation greenness (NDVI)²⁰, Enhanced Vegetation Index (EVI)²¹, solar-induced vegetation fluorescence (solar-induced chlorophyll fluorescence, SIF)²²), or when daily mean air temperature ($T_{\text{mean}}^{\text{air}}$) is used instead of daily maximum air temperature ($T_{\text{max}}^{\text{air}}$) to calculate $T_{\text{opt}}^{\text{eco}}$ (Supplementary Figs. 3–6; see also Methods). Note that although the covariance between air temperature, atmospheric VPD and solar radiation may confuse the direct effect of air temperature on vegetation productivity, we verified that neither VPD nor radiation is the dominant factor determining the pattern of $T_{\text{opt}}^{\text{eco}}$ at the global scale (see Methods).

To test the second hypothesis, we compared satellite-derived $T_{\text{opt}}^{\text{eco}}$ with $T_{\text{opt}}^{\text{leaf}}$ from the responses of maximum Rubisco-limited carboxylation rates (V_{cmax}) to temperature from leaf-scale measurements for 36 species⁵. Note that the $T_{\text{opt}}^{\text{leaf}}$ here refers to the temperature optima for leaf-scale (gross) photosynthetic capacity rather than for

leaf net photosynthesis, which equals gross photosynthesis minus photorespiration and minus dark respiration (for more details, see Methods). We found that $T_{\text{opt}}^{\text{eco}}$ is lower than $T_{\text{opt}}^{\text{leaf}}$ (Supplementary Fig. 7). This difference may originate from $T_{\text{opt}}^{\text{eco}}$ being additionally limited by high VPD during hot and dry periods⁶ and by soil-moisture deficits during extensive dry episodes²³, under real-world conditions. Under conditions of high temperature, atmospheric VPD increases while soil moisture decreases. Stomatal conductance, and hence carbon assimilation rates (GPP at ecosystem scale), decrease to prevent exceedingly low leaf-water potentials and any resulting plant tissue damage from cavitation²⁴. In contrast, leaf-level photosynthesis measurements that determine the temperature response curve of V_{cmax} are usually performed in absence of water stress by maintaining relatively low VPD conditions (for example, refs. 25–30), unless the research objective is to investigate drought effect on leaf photosynthetic parameters (as in refs. 31,32). In addition, plant phenology controls leaf age, vitality (photosynthetic rates) and foliar density (for example, Leaf Area Index, LAI)³³, and may therefore co-determine ecosystem-level temperature limitations and the optimum temperature for canopy photosynthesis³⁴. It is also important to note when comparing $T_{\text{opt}}^{\text{leaf}}$ with $T_{\text{opt}}^{\text{eco}}$ that leaf-scale measurements are often limited to sunlit leaves, which could lead to a positive bias of existing in situ $T_{\text{opt}}^{\text{leaf}}$ measurements. Furthermore, the tree species database used by Kattge and Knorr⁵ from which $T_{\text{opt}}^{\text{leaf}}$ data were collected does not include any tropical species. This may explain why global models prescribed with $T_{\text{opt}}^{\text{leaf}}$ give divergent results for tropical biomes.

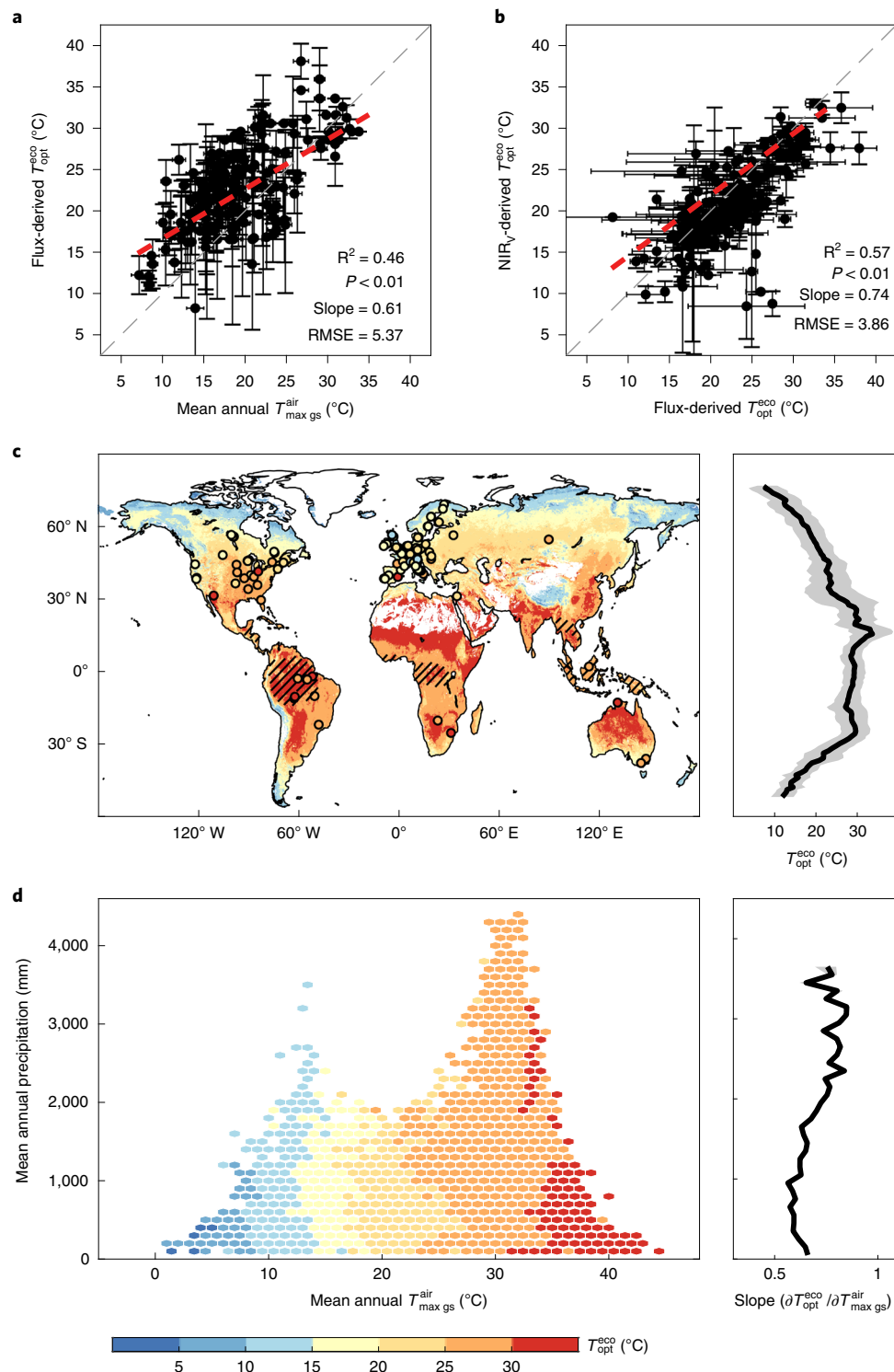
The relationship between $T_{\text{opt}}^{\text{eco}}$ and background climate is shown in Fig. 1d. The sampling of leaf-scale studies does not provide consistent evidence about the dependence of $T_{\text{opt}}^{\text{leaf}}$ on climate, and there are positive correlations between $T_{\text{opt}}^{\text{leaf}}$ and growing-season air temperature in a set of studies^{1,5,35–37} attributed to evolutionary adaptation³⁸, but no clear relationship between $T_{\text{opt}}^{\text{leaf}}$ and growth temperature^{39–41}. In contrast, $T_{\text{opt}}^{\text{eco}}$ inferred from satellite GPP proxies in our study increases with $T_{\text{max gs}}^{\text{air}}$ across the globe. In temperature–precipitation space, the spatial sensitivity of $T_{\text{opt}}^{\text{eco}}$ to $T_{\text{max gs}}^{\text{air}}$ (the slope of the linear regression between these two variables) is lower than 1 for any precipitation bin (Fig. 1d), suggesting that spatial gradients of $T_{\text{opt}}^{\text{eco}}$ are smaller than those of $T_{\text{max gs}}^{\text{air}}$, possibly because hydraulic and phenological limitations further limit $T_{\text{opt}}^{\text{eco}}$ across spatial gradients. In fact, the spatial sensitivity of $T_{\text{opt}}^{\text{eco}}$ to $T_{\text{max gs}}^{\text{air}}$ generally increases with increasing mean annual precipitation (Fig. 1d), even though $T_{\text{opt}}^{\text{eco}}$ is not significantly correlated with precipitation after controlling for the effect of $T_{\text{max gs}}^{\text{air}}$ (Fig. 1d). This thermal adaptation of $T_{\text{opt}}^{\text{eco}}$, suggested by the positive spatial slope of the $T_{\text{opt}}^{\text{eco}}$ –air temperature relation, is also observed across biomes. As shown in Fig. 2, there

Fig. 1 | Distribution of $T_{\text{opt}}^{\text{eco}}$ for vegetation productivity derived from flux-tower sites and satellite-based data for near-infrared reflectance of vegetation (NIR_v). **a**, Relationship between mean annual daily maximum air temperature averaged over the growing season ($T_{\text{max gs}}^{\text{air}}$) and $T_{\text{opt}}^{\text{eco}}$ derived from daily measurements of photosynthesis across eddy covariance sites. Flux-derived $T_{\text{max gs}}^{\text{air}}$ and $T_{\text{opt}}^{\text{eco}}$ were both obtained using observations from flux towers. Error bars indicate \pm s.d. The dotted grey line represents $y=x$ and the dotted red line is $y=0.61x+10.65$, which is derived by linear regression with the statistical significance of the slope, or its P -value, given by Student's t -test. **b**, Relationship between $T_{\text{opt}}^{\text{eco}}$ derived from flux data and $T_{\text{opt}}^{\text{eco}}$ derived from NIR_v data. For each site, we extracted and averaged $T_{\text{opt}}^{\text{eco}}$ values within a 3×3 pixel window around the site from NIR_v -derived $T_{\text{opt}}^{\text{eco}}$ map and calculated the s.d. of nine $T_{\text{opt}}^{\text{eco}}$ values within the window. Error bars indicate \pm s.d. The dotted grey line represents $y=x$ and the dotted red line is $y=0.74x+7.10$, which is derived by linear regression with the statistical significance of the slope, or its P -value, given by Student's t -test. **c**, Spatial distribution of $T_{\text{opt}}^{\text{eco}}$ for vegetation productivity (left panel) and $T_{\text{opt}}^{\text{eco}}$ averaged by latitude (right panel). $T_{\text{opt}}^{\text{eco}}$ is determined using NIR_v data calculated on the basis of satellite observations from moderate resolution imaging spectroradiometer (MODIS). Note that only gridded pixels with annual mean normalized difference vegetation index (NDVI) value larger than 0.1 and detectable $T_{\text{opt}}^{\text{eco}}$ are shown here. Areas of tropical forests based on current vegetation distribution are indicated by hatching. The circles on the map are coloured according to the local value of $T_{\text{opt}}^{\text{eco}}$ retrieved from GPP at the location of each flux site. The solid line and shaded area in the right panel indicate the mean and s.d., respectively, of $T_{\text{opt}}^{\text{eco}}$ summarized by latitude. **d**, $T_{\text{opt}}^{\text{eco}}$ in the climate space (left panel) and the temperature sensitivity of $T_{\text{opt}}^{\text{eco}}$ along the precipitation gradient (right panel). Each climate bin is defined by 1-°C intervals of $T_{\text{max gs}}^{\text{air}}$ and 100-mm intervals of mean annual precipitation, based on current climate conditions averaged between 2001 and 2013. The solid line in the right panel represents the temperature sensitivity of $T_{\text{opt}}^{\text{eco}}$ along the precipitation gradient, calculated as the slope of the linear regression between $T_{\text{opt}}^{\text{eco}}$ and $T_{\text{max gs}}^{\text{air}}$ for a given precipitation level. The shaded area indicates the s.d. of temperature sensitivity of $T_{\text{opt}}^{\text{eco}}$ estimated by bootstrapping. The s.d. of temperature sensitivity of $T_{\text{opt}}^{\text{eco}}$ is smaller than or equal to 0.02 °C per °C when mean annual precipitation is below 3,000 mm.

is a significant positive correlation between T_{opt}^{eco} and $T_{max\ gs}^{air}$ with a slope of 0.76 across different biomes. Among biomes, the largest mean T_{opt}^{eco} is found in tropical evergreen broadleaved forest (EBF) ($29 \pm 3^\circ\text{C}$), and the smallest mean T_{opt}^{eco} ($13 \pm 3^\circ\text{C}$) in cold grasslands covering the Tibetan Plateau (Fig. 2 and Supplementary Fig. 8).

Results from both model simulations and very limited observational studies suggest a decrease in canopy photosynthesis of tropical forests at high temperature^{15,42–45}, which led us to formulate the third hypothesis of tropical forests already operating at T_{opt}^{eco} close to $T_{max\ gs}^{air}$, implying that canopy photosynthesis may

decrease under future warming^{15,16}. This hypothesis is verified from the data shown in Fig. 3 (see also Supplementary Fig. 9). T_{opt}^{eco} is indeed slightly lower (1.4°C) than $T_{max\ gs}^{air}$ over tropical evergreen forests, suggesting a small safety margin for canopy photosynthesis under future warming. Note that the safety margin could become larger than that suggested by the air temperature data if leaf thermal regulation acclimatises to the warming air temperature (see Methods). In contrast, arctic (north of 65°N) and boreal (50°N – 65°N) ecosystems exhibit substantially larger safety margins, that is, a larger positive difference between T_{opt}^{eco} and $T_{max\ gs}^{air}$



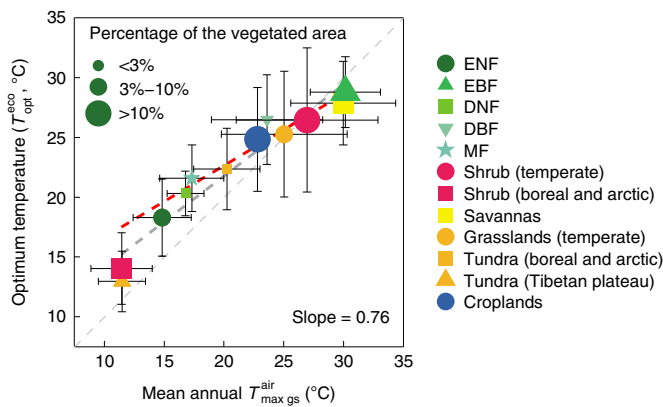


Fig. 2 | Relationship between $T_{\max gs}^{\text{air}}$ and $T_{\text{opt}}^{\text{eco}}$ across vegetation types. The error bars indicate the s.d. of $T_{\text{opt}}^{\text{eco}}/T_{\max gs}^{\text{air}}$ for each vegetation type: ENF, evergreen needle-leaved forest; EBF, evergreen broad-leaved forest; DNF, deciduous needle-leaved forest; DBF, deciduous broadleaved forest; MF, mixed forest; Shrub, closed and open shrublands. The light grey dotted line represents $y=x$. The dark-grey dotted line is $y=0.76x+6.48$ derived by linear regression, with the slope value (estimated using Student's t -test) shown in the bottom right. The red dotted line is the flux-tower derived slope (0.61) from Fig. 1a. The size of each symbol corresponds to the three categories (<3%, 3–10% and >10%) of occupied vegetated area on land.

(Fig. 3a and Supplementary Fig. 9). Analyses of the 16-day averaged T_{\max}^{air} distribution during the period when $T_{\text{opt}}^{\text{eco}}$ is observed show that the rank of $T_{\text{opt}}^{\text{eco}}$ in the T_{\max}^{air} distribution is already near the highest quantile of T_{\max}^{air} (>70%) for tropical evergreen forests (Supplementary Fig. 10). Based on this result, one may expect that rising air temperature in the future, irrespective of the indirect effect of increasing VPD, may limit or decrease vegetation productivity in tropical forests, but not in temperate or boreal ecosystems.

Global terrestrial daily maximum air temperature is projected to rise by 1.9°C under the representative concentration pathway

(RCP)2.6 low-warming climate scenario and by 5.6°C under the RCP8.5 scenario by 2100⁴⁶. We compared these $T_{\max gs}^{\text{air}}$ projections with the present-day distribution of $T_{\text{opt}}^{\text{eco}}$ with a focus on tropical evergreen forests, where optimum temperature is currently just below the limit of $T_{\max gs}^{\text{air}}$ (see Methods; Figs. 3b,c). The key uncertainty in this discussion is, however, whether or not $T_{\text{opt}}^{\text{eco}}$ will acclimate and follow the increase in $T_{\max gs}^{\text{air}}$. We therefore looked at possible acclimation from time series of $T_{\text{opt}}^{\text{eco}}$ retrieved from the advanced very high resolution radiometer (AVHRR) NDVI, which spans the last 30 years and comprises almost a 1°C temperature range. NDVI-derived $T_{\text{opt}}^{\text{eco}}$ did not have a significant trend over the last three decades except for the northern lands (north of 60°N) where warming is more pronounced⁴⁷ (Supplementary Fig. 11). This suggests that the recent 1°C warming is not large enough to elicit an acclimation response from some ecosystems, given decadal variability⁴⁸. In addition, the annual $T_{\text{opt}}^{\text{eco}}$ derived from flux sites estimates of GPP did not exhibit a positive trend and was not significantly correlated with annual variations of $T_{\max gs}^{\text{air}}$, although the flux time series are probably too short to properly evaluate trends of $T_{\text{opt}}^{\text{eco}}$ related to possible acclimation processes (Supplementary Fig. 12). Because we detected no indication for its existence, we first assumed no acclimation in the comparison of future $T_{\max gs}^{\text{air}}$ projections from climate models with the current distribution of $T_{\text{opt}}^{\text{eco}}$. Under this assumption, the average $T_{\max gs}^{\text{air}}$ of tropical evergreen forests will exceed the current value of $T_{\text{opt}}^{\text{eco}}$ for RCP2.6 by 2.6°C, and by 5.7°C for RCP8.5 (Fig. 3c). On the other hand, boreal and arctic biomes will still remain within the safety margin, with $T_{\text{opt}}^{\text{eco}}$ staying above $T_{\max gs}^{\text{air}}$, except under the RCP8.5 high-warming scenario (Fig. 3b and Supplementary Fig. 13).

Despite the lack of in situ observational evidence for GPP acclimation to the ongoing warming trend, we tested a simple future acclimation scenario based on the space-for-time substitution approach⁴⁹, as applied in several studies using observed spatial gradients to hindcast temporal changes^{50,51}. Here, we assume that temporal change of $T_{\text{opt}}^{\text{eco}}$ will evolve proportionally to $T_{\max gs}^{\text{air}}$, following the spatial temperature sensitivity of $T_{\text{opt}}^{\text{eco}}$ to $T_{\max gs}^{\text{air}}$ in Fig. 1d and the indirect effects of temperature increase (for example, by increasing VPD) are excluded. We took the differences in

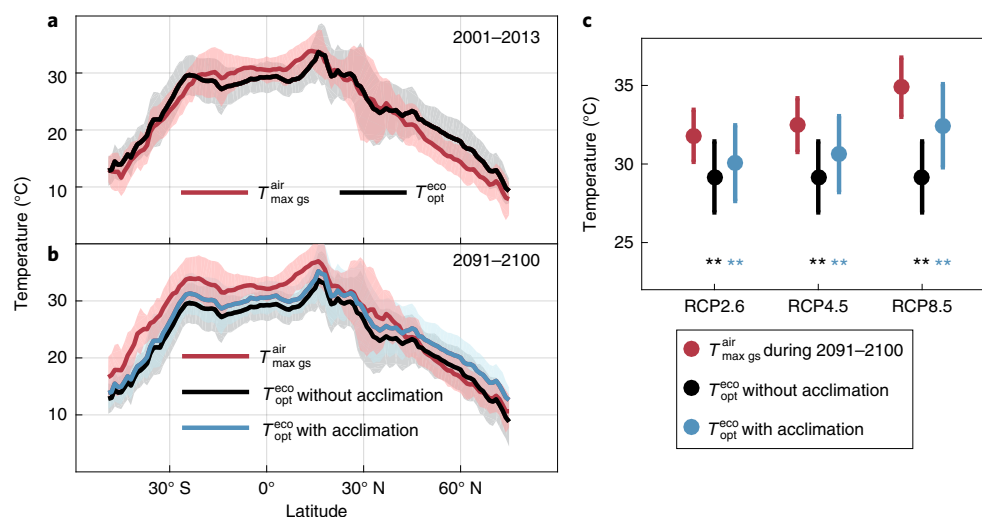


Fig. 3 | Change with latitude in $T_{\text{opt}}^{\text{eco}}$ and $T_{\max gs}^{\text{air}}$. **a**, Current $T_{\text{opt}}^{\text{eco}}$ versus current $T_{\max gs}^{\text{air}}$. **b**, Future $T_{\text{opt}}^{\text{eco}}$ versus future $T_{\max gs}^{\text{air}}$. Current $T_{\text{opt}}^{\text{eco}}$ and $T_{\max gs}^{\text{air}}$ are calculated using current temperature for 2001–2013, whereas acclimated $T_{\text{opt}}^{\text{eco}}$ and future $T_{\max gs}^{\text{air}}$ are first calculated pixel by pixel using temperature for 2091–2100, projected by general circulation models (GCM) under the RCP4.5 scenario and then averaged by latitude. Acclimated $T_{\text{opt}}^{\text{eco}}$ is determined based on the projected temperature and temperature sensitivity of $T_{\text{opt}}^{\text{eco}}$ using the annual precipitation level predicted for 2091–2100. The solid line and shaded area in each panel indicate the mean and s.d., respectively, of $T_{\text{opt}}^{\text{eco}}$ or $T_{\max gs}^{\text{air}}$ summarized by latitude. **c**, Future $T_{\text{opt}}^{\text{eco}}$ versus future $T_{\max gs}^{\text{air}}$ for tropical evergreen forests. ** indicates that $T_{\text{opt}}^{\text{eco}}$ is significantly lower than $T_{\max gs}^{\text{air}}$ at $P < 0.01$ in a paired t -test. Error bars indicate \pm s.d.

precipitation levels into account, so that areas that become wetter also exhibit faster acclimation. Even with this assumed acclimation law, $T_{\max\text{gs}}^{\text{air}}$ will still surpass $T_{\text{opt}}^{\text{eco}}$ by 1.7°C under RCP2.6 and by 2.5°C under RCP8.5 for tropical evergreen forests (Fig. 3c). Not accounting for precipitation levels in the acclimation rates produced similar results (Supplementary Figs. 14 and 15).

Our global-scale analysis of $T_{\text{opt}}^{\text{eco}}$ derived from globally distributed point measurements of eddy covariance and space-borne observations of proxies of vegetation productivity is an attempt to diagnose the global distribution of ecosystem-scale temperature optima of photosynthesis. It should be noted, however, that hypotheses about thermal acclimation of $T_{\text{opt}}^{\text{eco}}$ are still highly uncertain because ecosystem adjustments can lag substantially behind the rate of future warming, particularly for forests. More studies using datasets with longer time spans are needed in the future to more accurately detect eventual thermal acclimation of $T_{\text{opt}}^{\text{eco}}$. Furthermore, the acclimation of plants to increasing atmospheric CO₂ concentration and to changes in other environmental factors (for example, VPD) was also not considered in the current analyses. Constraining the spatially observed temperature sensitivity of $T_{\text{opt}}^{\text{eco}}$ over time is a priority for future studies. Continuous monitoring and dedicated manipulative experiments could improve our understanding on the features of $T_{\text{opt}}^{\text{eco}}$ and thermal acclimation in earth system models⁵².

Methods

FLUXNET data. The half-hourly eddy covariance GPP data were obtained from FLUXNET datasets, and were quality-controlled, filtered against low turbulence, and gap-filled using consistent methods, as described in ref. ³³ Only freely available FLUXNET data were used in this study. All the half-hourly GPP data were aggregated into daily-accumulated GPP for further estimates of the optimal temperature for vegetation productivity. Daily maximum air temperature (T_{\max}^{air}) was determined as the maximum air temperature value from all the half-hourly air temperature observations. We included only site-years with more than 80% of half-hourly data available. A total of 153 individual FLUXNET sites with 663 site-years of GPP data were used in this study.

NIR_v. An approach was recently proposed for estimating vegetation photosynthetic capacity by remote sensing, that is, the NIR_v, which can differentiate between the confounding effects of background brightness, leaf area and the distribution of photosynthetic capacity with depth in canopies¹⁹. NIR_v is calculated as the product of NIR_r and NDVI¹⁹. As a proxy of photosynthesis, NIR_v is suggested to be strongly correlated with solar-induced chlorophyll fluorescence (SIF), a direct index of photons intercepted by chlorophyll, and shows higher correlation with observed GPP than NDVI¹⁹. We used satellite-derived NIR_v to calculate and map the optimal air temperature for vegetation productivity at an ecosystem scale ($T_{\text{opt}}^{\text{eco}}$). Following ref. ¹⁹, we calculated 16-day NIR_v for 2001–2013 as the product of MODIS 16-day NIR reflectance and MODIS 16-day NDVI, both of which were derived from the MOD13A2 Vegetation Index Product with a spatial resolution of 1 km. Only positive NIR_v values were used in the analysis.

NDVI. The NDVI is a vegetation index defined as the ratio of the difference between NIR and red visible reflectance to their sum, and is widely used to represent vegetation greenness⁶⁴. To account for uncertainties from different satellite datasets, three independent NDVI datasets were used, including bi-weekly NDVI data from Global Inventory Modeling and Mapping Studies (GIMMS) AVHRR, 16-day NDVI data from terra MODIS and 10-day NDVI data from Satellite Pour l'Observation de la Terre Vegetation (SPOT Vegetation). The three NDVI datasets spanned three decades: 1982–2009 for AVHRR NDVI datasets, 2000–2009 for MODIS NDVI datasets and 1999–2009 for SPOT NDVI datasets, with the spatial resolutions of 8 km, 1 km, and 1 km, respectively. All NDVI datasets have been corrected to reduce the effects of volcanic aerosols, solar angle and sensor errors^{20,55,56}. Pixels with a mean annual NDVI > 0.1 were defined as the vegetated area for each dataset.

EVI. EVI is another vegetation index designed to enhance the vegetation signal by minimizing canopy–soil variations and to improve sensitivity over dense vegetation conditions⁵¹, and is found to correlate well with estimated GPP on a site-by-site basis⁵⁷. We used a 16-day EVI dataset for 2000–2009 with a spatial resolution of 1 km from the MOD12A1 Vegetation Index Product. Effects from aerosols, solar angle and sensor error have all been corrected²¹.

SIF. Chlorophylls in plants absorb short-wave radiation and dissipates excess energy as light or heat. The long-wave radiation re-emitted by chlorophylls is referred as chlorophyll fluorescence. Recent studies have reported that remotely

sensed SIF could serve as an indicator of photosynthesis rate and it is correlated with model-simulated GPP⁵⁸. Following previous studies^{58,59}, we retrieved SIF from two different retrieval windows, 757 nm and 771 nm, as well as two polarization states, S and P, using a Fourier transform spectrometer on the Japanese Greenhouse gases Observing SATellite (GOSAT)²⁰. These diverse SIF samples were then aggregated into monthly gridded data at a spatial resolution of 2° from June 2009 to June 2012.

Vegetation distribution. We used MODIS land cover with the classification scheme of the International Geosphere-Biosphere Programme (IGBP). The MODIS IGBP land cover data were derived from the MOD12Q1 Land Cover Science Data Product at a spatial resolution of 1 km and an updated digital Köppen–Geiger world map of climatic classification⁶⁰. Within the vegetated area defined by NDVI thresholds, the 17 land cover types were reclassified into 9 vegetation types: ENF, EBF, DNF, DBF, ME, savannas, cropland, grassland and shrubland. Based on the main climates in the world map of the Köppen–Geiger climatic classification⁶⁰, grassland was further subdivided into temperate grasslands, boreal and arctic tundra, and shrubland was further subdivided into temperate and boreal shrubland. The grassland over the Tibetan Plateau was considered separately because the Tibetan Plateau has an average altitude higher than 4,000 m above sea level⁶¹, and thus a unique alpine climate. In contrast to temperate grasslands and shrubland, where water is a major limiting factor for vegetation productivity, alpine ecosystems on the Tibetan Plateau are mainly limited by thermal conditions⁶².

Climate dataset. The gridded air temperature and precipitation data for 1982 to 2013 were obtained from the Climatic Research Unit/National Centers for Environmental Protection (CRU/NCEP) 6-hourly dataset with a spatial resolution of 0.5°. Note that the purpose of this study is to investigate the optimal air temperature for photosynthesis. Optimal leaf temperature is also of interest; however, it was not addressed in this study because accurate canopy-integrated measurements of leaf temperatures are not available at the eddy covariance sites and at a global scale as gridded datasets. For a discussion about calculation of temperature optimum from air temperature and from surface temperature, we used remotely sensed land surface temperature (LST), which is inverted from infrared emissivity measured by MODIS (MYD11A2 version 6). This dataset had an original spatial resolution of 1 km, spanning from July 2002 to December 2014. The error of the MODIS LST product, which primarily stems from cloud contamination and emissivity uncertainties, was reported to be less than 3°C⁶³. Generally, the occurrence time of $T_{\max}^{\text{surface}}$ (14:00–16:00) is relatively close to the Aqua overpass time (13:30), and thus we assumed that $T_{\max}^{\text{surface}}$ from MODIS-Aqua is comparable with the daily maximum leaf surface temperature (T_{\max}^{leaf}). Corresponding to the temporal resolutions of MODIS, AVHRR and SPOT datasets, the 6-hourly climate data were aggregated into 16-day, biweekly and 10-day values, respectively, before further analyses. Given the different spatial resolutions of satellite observations and climate data, we extracted time series of daily maximum air temperature and precipitation from the aggregated CRU/NCEP data for each pixel of the sets of remotely sensed data. The daily maximum air temperature (T_{\max}^{air}) of the growing season averaged from 2001 to 2013 was calculated as the current mean growing-season daily maximum air temperature ($T_{\max\text{gs}}^{\text{air}}$). Information on the growing season was derived from the study by ref. ⁶⁴, which was determined from the GIMMS Leaf Area Index dataset (GIMMS LAI_{3g}) using a Savitzky–Golay filter and then refined by excluding the ground-freeze period identified by the freeze/thaw earth system data record (see details in ref. ⁶⁴). We also documented the temperature thresholds at which the growing season begins and ends for each year. Temperature thresholds were averaged from 2001 to 2013 for the onset and end of the growing season, respectively. We also applied Water and Global Change (WATCH) Forcing Data (WFD) methodology to ERA-interim (WFDEI) data with a temporal resolution of 3 hours⁶⁵.

We used climate projections for the end of the twenty-first century (2091–2100) using 20 models that participated in the phase five of coupled model intercomparison project (CMIP5) under the RCP2.6, RCP4.5 and RCP8.5 scenarios⁶⁶ to determine the impact of future warming on vegetation productivity (see model list in Supplementary Table 2). Considering the mismatch between CRU/NCEP datasets and outputs from GCM for current climate conditions, we generated future temperature and precipitation maps by adding the relative changes in GCM-derived climate projections to the current climate for each pixel. $T_{\max\text{gs}}^{\text{air}}$ for the late twenty-first century was estimated using the same temperature thresholds as for the current $T_{\max\text{gs}}^{\text{air}}$. All GCM projections were resampled to a resolution of 1° using a first-order conservative interpolation method⁶⁶.

Analysis. We estimated local $T_{\text{opt}}^{\text{eco}}$ by examining the temperature response curve of MODIS NIR_v. Following refs. ^{37,18}, NIR_v time series throughout the entire monitoring period and the corresponding temperature data were grouped into 1°C temperature bins for each pixel within vegetated areas, which were defined as regions with a mean annual NDVI value larger than 0.1. We used the 90% quantile of the NIR_v data as the response of NIR_v within each temperature bin due to the potential influences of other environmental constraints such as clouds and droughts. We then calculated the running means of every three temperature bins

to develop the temperature response curve of NIR_v . The T_{opt}^{eco} was determined from the response curve at which NIR_v was maximized (Supplementary Fig. 16). Note that T_{opt}^{eco} may not be detected for some pixels where the maximum NIR_v was only attained at either end of the response curve, accounting for 3.5% of the vegetated areas. Only vegetated areas with detectable T_{opt}^{eco} were shown when mapping the spatial pattern of T_{opt}^{eco} . The derivation of T_{opt}^{eco} is robust to the choice of a particular climate-forcing dataset (Supplementary Fig. 2). Instead of using the temperature corresponding to the maximum 90th quantile NIR_v to calculate T_{opt}^{eco} , we also applied nonlinear regression of the photosynthetic temperature response data (equation (1)) to estimate T_{opt}^{eco} , which produced similar results (Supplementary Fig. 2):

$$NIR_v(T) = NIR_{v(OPT)} - b(T - T_{opt}^{eco})^2 \quad (1)$$

where $NIR_{v(T)}$ is the NIR_v value at a daily maximum temperature T and b is a parameter describing the spread of the parabola^{48,67}. T_{opt}^{eco} is the vertex of each fit and $NIR_{v(OPT)}$ is the NIR_v value at T_{opt}^{eco} . Finally, we used daily mean air temperature (T_{mean}^{air}) instead of T_{max}^{air} to calculate T_{opt}^{eco} . In this test, T_{opt}^{eco} derived from T_{mean}^{air} is smaller than T_{opt}^{eco} estimated from T_{max}^{air} , but the two variables were strongly spatially correlated (Supplementary Fig. 6).

We investigated the relationship between T_{opt}^{eco} and climate variables by averaging T_{opt}^{eco} in the climate space with 1 °C intervals of mean annual T_{max}^{air} averaged over the growing season ($T_{max}^{air}_{gs}$) and 100 mm intervals of mean annual precipitation (MAP) (Fig. 1d). For each MAP interval, we calculated the apparent spatial sensitivity of T_{opt}^{eco} in response to changes in $T_{max}^{air}_{gs}$ using bootstrapping method. We performed the linear regression analysis 1,000 times by randomly selecting a subset of 80% of the samples from pairs of T_{opt}^{eco} and $T_{max}^{air}_{gs}$ within each MAP interval. The mean and s.d. of the temperature sensitivity of T_{opt}^{eco} were subsequently estimated along the MAP gradient.

Air temperature, atmospheric VPD and solar radiation usually co-vary in time and space, so that the empirical observation of spatial patterns of T_{opt}^{eco} in this study cannot be unambiguously attributed to air temperature as a single explaining factor of T_{opt}^{eco} . Under conditions of high temperature, atmospheric VPD increases, soil moisture decreases with a lag, and stomatal conductance and hence carbon assimilation rates (GPP at the ecosystem scale) decrease to prevent exceedingly low leaf-water potentials and resulting plant tissue damage from cavitation²⁴. We show that across climatic gradients T_{opt}^{eco} is systematically higher at high maximum air temperatures, but not systematically lower at high VPD conditions (Supplementary Fig. 17). We then calculated the variance inflation factor (VIF) between VPD and $T_{max}^{air}_{gs}$ under each VPD bin in the regression model of:

$$T_{opt}^{eco} = k_0 + k_1 \times T_{max}^{air}_{gs} + k_2 \times VPD \quad (2)$$

where k_1 and k_2 is the apparent sensitivity of T_{opt}^{eco} to $T_{max}^{air}_{gs}$ and VPD, respectively, with a constant term k_0 . As shown in Supplementary Fig. 18, we observed that the VIF value ranged only between 1.001 and 1.438, suggesting relatively low multicollinearity between VPD and temperature. Even so, to examine whether VPD can substantially affect the relationship between T_{opt}^{eco} and $T_{max}^{air}_{gs}$, we further calculated the partial (intrinsic) sensitivity of T_{opt}^{eco} to $T_{max}^{air}_{gs}$ in each grid point based on the following bilinear regression:

$$T_{opt}^{eco} = k_0 + k_1 \times T_{max}^{air}_{gs} + k_2 \times VPD + k_3 \times VPD \times T_{max}^{air}_{gs} \quad (3)$$

where the partial sensitivity of T_{opt}^{eco} to $T_{max}^{air}_{gs}$ is defined as k_1 in equation (3) under each VPD bin. We then compared the partial sensitivity with the apparent sensitivity of T_{opt}^{eco} to $T_{max}^{air}_{gs}$ estimated using the previously mentioned linear regression between T_{opt}^{eco} and $T_{max}^{air}_{gs}$ for each VPD bin. As shown in Supplementary Fig. 19, although the apparent sensitivity of T_{opt}^{eco} to $T_{max}^{air}_{gs}$ is generally lower than the partial (intrinsic) sensitivity of T_{opt}^{eco} to $T_{max}^{air}_{gs}$, the apparent sensitivity to $T_{max}^{air}_{gs}$ remains positive, even when VPD is taken into account, except under very high VPD bins (higher than ~4.5 kPa) representing less than 1% of the study area. These results indicate that the patterns of T_{opt}^{eco} are not dominated by high VPD reducing canopy photosynthesis as an indirect effect of higher air temperature increasing VPD. Moreover, we also calculated the percentiles of downward short-wave solar radiation (Rad) at the time of year when T_{opt}^{eco} is observed for the 16-day averaged Rad distribution. As shown in Supplementary Fig. 20, the Rad value when T_{opt}^{eco} was retrieved from global observations was below the 95th percentile in the 16-day Rad distribution for ~80% of the study area, which is mainly in mid and low latitudes, such as Africa, India, Australia, eastern Brazil, and the south and southwest of North America. By comparison, for most boreal regions in parts of south China, southeast US, as well as in parts of South America, the timing of T_{opt}^{eco} is consistent with the time of maximum solar radiation. This is because T_{opt}^{eco} in these regions generally appears in summer, which is also the period when solar radiation is at its maximum during the year.

The NIR_v -derived T_{opt}^{eco} was compared with T_{opt}^{eco} estimated using GPP data from 153 eddy covariance sites. Flux-derived T_{opt}^{eco} was determined for each site-year with daily-accumulated GPP and corresponding temperature data from flux-tower observations. The same method to estimate local T_{opt}^{eco} using NIR_v datasets was

applied. A robust estimate of T_{opt}^{eco} can be derived for 125 sites (Supplementary Table 1). For each site, we calculated the mean and s.d. of T_{opt}^{eco} across different years. We then extracted and averaged T_{opt}^{eco} values within a 3×3 pixel window around each site from the NIR_v -derived T_{opt}^{eco} map, and calculated the s.d. of the nine T_{opt}^{eco} values within the window. The relationship between NIR_v - and flux-derived T_{opt}^{eco} was reported using a least-square linear regression, and the statistical significance of the slope, or its P -value, given by Student's t -test. The results show that NIR_v -derived T_{opt}^{eco} is comparable to that estimated independently from measurements of flux-tower eddy covariance (Fig. 1b).

We compared the spatial distribution of T_{opt}^{eco} derived from NIR_v with the one obtained from NDVI datasets. Consistent spatial patterns of T_{opt}^{eco} are derived from each of the three NDVI datasets (Supplementary Fig. 21). A global composite map of T_{opt}^{eco} (Supplementary Fig. 3) was then generated by averaging estimates derived from the three NDVI datasets. Given the inconsistent spatial resolutions of the different products, we resampled T_{opt}^{eco} to a common grid of 8 km before averaging. T_{opt}^{eco} from NDVI datasets generally show a spatial pattern similar to that from NIR_v , but with smaller NDVI-derived T_{opt}^{eco} values for central Australia and southern South America (Supplementary Fig. 3). We compared the spatial distribution of T_{opt}^{eco} derived from NIR_v with that from MODIS EVI data between 2001 and 2013, and found that the EVI-derived T_{opt}^{eco} showed very similar spatial pattern to that of NIR_v -derived T_{opt}^{eco} (Supplementary Fig. 4). The distribution of T_{opt}^{eco} derived from NIR_v and from GOSAT SIF datasets also have similar spatial patterns, even though the NIR_v -derived T_{opt}^{eco} is higher in tropical regions, particularly in cultivated areas of southeast Brazil (Supplementary Fig. 5).

At leaf scale, the photosynthesis-temperature response is suggested to be primarily controlled by three sets of processes: biochemical, respiratory and stomatal processes⁶⁸. Much of the effort to date to understand variability in the leaf-level photosynthesis-temperature response has focused on biochemical processes⁶⁸, with V_{max} and J_{max} being two major parameters controlling the maximum rates of photosynthesis limited by CO_2 and light, respectively⁶⁹. Therefore, in this study, we compared T_{opt}^{eco} derived using GPP proxies with leaf-scale optimal temperature of V_{max} , although GPP is, in theory, more comparable to net photosynthesis, that is, leaf gross photosynthesis minus photorespiration and minus dark respiration. Since photorespiration increases exponentially with temperature⁷⁰, the optimum temperature of GPP (T_{opt}^{eco}) should be lower than the optimal temperature of V_{max} . For this comparison to be made, we extracted and averaged T_{opt}^{eco} values within a 3×3 pixel window from the NIR_v -derived T_{opt}^{eco} map around the reported site location (longitude and latitude) of leaf-scale measurements. For leaf-scale measurements without the information of site location, we calculated the average NIR_v -derived T_{opt}^{eco} values across pixels with both the same growing-season mean temperature and the same plant functional type as the corresponding site.

T_{opt}^{eco} is different from T_{opt}^{leaf} not only because of respiratory process, but also because air temperature can differ from leaf temperatures⁷¹, which are regulated by leaf traits affecting the leaf energy balance⁷². Because, to our knowledge, global gridded monthly leaf temperature data are not available, we used daily maximum LST (T_{max}^{surf}) from MODIS to calculate $T_{opt}^{eco-LST}$ to illustrate the potential differences between $T_{opt}^{eco-LST}$ and T_{opt}^{eco} . As shown in Supplementary Fig. 22, the $T_{opt}^{eco-LST}$ is similar to T_{opt}^{eco} over tropical savannas. However, over moist tropical forests $T_{opt}^{eco-LST}$ is lower than T_{opt}^{eco} , which can be explained by the lower daytime surface temperature than air temperature as a result of strong evapotranspiration effects^{71,73}. This ecosystem-dependent difference between $T_{opt}^{eco-LST}$ and T_{opt}^{eco} suggests that the leaf thermal regulation mechanism through the physiological and morphological changes⁷² is an important ecosystem process that shapes spatial variations of T_{opt}^{eco} . In addition, if the difference between leaf temperature and air temperature increases in response to warmer air temperatures (that is, if leaf thermal regulation acclimates to warmer temperature), the safety margin of tropical ecosystems would increase more than the air temperature data currently suggests. However, the long-term in situ leaf temperature data required to test this hypothesis independently are currently not available.

To account for potential changes in T_{opt}^{eco} under future warming, we estimated the acclimated T_{opt}^{eco} for vegetation productivity by the end of the twenty-first century (2091–2100) using recent IPCC climate projections⁴⁶. To this end, we applied the space-for-time substitution approach⁴⁹, assuming that temporally T_{opt}^{eco} will evolve proportionally to $T_{max}^{air}_{gs}$ following the spatial temperature sensitivity of T_{opt}^{eco} to $T_{max}^{air}_{gs}$. Given the relatively large uncertainties of precipitation projections, we considered two future precipitation scenarios. For the first scenario, we estimated acclimated T_{opt}^{eco} pixel by pixel using the temperature sensitivity of T_{opt}^{eco} under the present MAP level, assuming that MAP does not change before the end of the twenty-first century. For the second scenario, we accounted for MAP and the acclimated T_{opt}^{eco} was calculated pixel by pixel using the temperature sensitivity of T_{opt}^{eco} under the projected MAP level for 2091–2100. Acclimated T_{opt}^{eco} was averaged across the GCMs under each scenario. Latitudinal variation of future T_{opt}^{eco} was derived by averaging within 1°-latitude bins from future T_{opt}^{eco} maps and then compared to future $T_{max}^{air}_{gs}$ summarized by latitude from future $T_{max}^{air}_{gs}$ maps.

Reporting summary. Further information on research design is available in the Nature Research Reporting Summary linked to this article.

Data availability

All data are available in the main text or the supplementary information. All computer codes used in this study can be provided by the corresponding author upon reasonable request.

Received: 4 October 2018; Accepted: 5 February 2019;

Published online: 11 March 2019

References

- Berry, J. & Björkman, O. Photosynthetic response and adaptation to temperature in higher plants. *Ann. Rev. Plant Physiol.* **31**, 491–543 (1980).
- Hughes, L. Biological consequences of global warming: is the signal already apparent? *Trends Ecol. Evol.* **15**, 56–61 (2000).
- Niu, S. et al. Climatic warming changes plant photosynthesis and its temperature dependence in a temperate steppe of northern China. *Environ. Exp. Bot.* **63**, 91–101 (2008).
- Way, D. A. & Yamori, W. Thermal acclimation of photosynthesis: on the importance of adjusting our definitions and accounting for thermal acclimation of respiration. *Photosynth. Res.* **119**, 89–100 (2014).
- Kattge, J. & Knorr, W. Temperature acclimation in a biochemical model of photosynthesis: a reanalysis of data from 36 species. *Plant Cell Environ.* **30**, 1176–1190 (2007).
- Lloyd, J. & Farquhar, G. D. Effects of rising temperatures and [CO₂] on the physiology of tropical forest trees. *Philos. T. Roy. Soc. B* **363**, 1811–1817 (2008).
- Medlyn, B. et al. Temperature response of parameters of a biochemically based model of photosynthesis. II. A review of experimental data. *Plant Cell Environ.* **25**, 1167–1179 (2002).
- Field, C. B., Randerson, J. T. & Malmström, C. M. Global net primary production: combining ecology and remote sensing. *Remote Sens. Environ.* **51**, 74–88 (1995).
- Niinemets, Ü. Global-scale climatic controls of leaf dry mass per area, density, and thickness in trees and shrubs. *Ecology* **82**, 453–469 (2001).
- Williams, A. P. et al. Temperature as a potent driver of regional forest drought stress and tree mortality. *Nat. Clim. Change* **3**, 292–297 (2013).
- Tyree, M. T. & Dixon, M. A. Water stress induced cavitation and embolism in some woody plants. *Physiol. Plantarum* **66**, 397–405 (1986).
- Yin, X. & Struik, P. C. C₃ and C₄ photosynthesis models: an overview from the perspective of crop modelling. *NJAS-Wagen. J. Life Sc.* **57**, 27–38 (2009).
- Smith, N. G., Malyshev, S. L., Shevliakova, E., Kattge, J. & Dukes, J. S. Foliar temperature acclimation reduces simulated carbon sensitivity to climate. *Nat. Clim. Change* **6**, 407–411 (2016).
- Mercado, L. M. et al. Large sensitivity in land carbon storage due to geographical and temporal variation in the thermal response of photosynthetic capacity. *New Phytol.* **218**, 1462–1477 (2018).
- Corlett, R. T. Impacts of warming on tropical lowland rainforests. *Trends Ecol. Evol.* **26**, 606–613 (2011).
- Doughty, C. E. & Goulden, M. L. Are tropical forests near a high temperature threshold? *J. Geophys. Res. Biogeophys.* **113**, G00B07 (2008).
- Baldocchi, D. et al. FLUXNET: a new tool to study the temporal and spatial variability of ecosystem-scale carbon dioxide, water vapor, and energy flux densities. *B. Am. Meteorol. Soc.* **82**, 2415–2434 (2001).
- Niu et al. Thermal optimality of net ecosystem exchange of carbon dioxide and underlying mechanisms. *New Phytol.* **194**, 775–783 (2012).
- Badgley, G., Field, C. B. & Berry, J. A. Canopy near-infrared reflectance and terrestrial photosynthesis. *Sci. Adv.* **3**, e1602244 (2017).
- Pinzon, J. E. & Tucker, C. J. A non-stationary 1981–2012 AVHRR NDVI_{3g} time series. *Remote Sens.* **6**, 6929–6960 (2014).
- Huete, A. et al. Overview of the radiometric and biophysical performance of the MODIS vegetation indices. *Remote Sens. Environ.* **83**, 195–213 (2002).
- Joiner, J., Yoshida, Y., Vasilkov, A. & Middleton, E. First observations of global and seasonal terrestrial chlorophyll fluorescence from space. *Biogeosciences* **8**, 637–651 (2011).
- Ma, S. et al. Photosynthetic responses to temperature across leaf-canopy-ecosystem scales: a 15-year study in a Californian oak-grass savanna. *Photosynth. Res.* **132**, 277–291 (2017).
- Stocker, B. D. et al. Quantifying soil moisture impacts on light use efficiency across biomes. *New Phytol.* **218**, 1430–1449 (2018).
- Bunce, J. A. Acclimation of photosynthesis to temperature in eight cool and warm climate herbaceous C₃ species: temperature dependence of parameters of a biochemical photosynthesis model. *Photosynth. Res.* **63**, 59–67 (2000).
- Han, Q., Kawasaki, T., Nakano, T. & Chiba, Y. Spatial and seasonal variability of temperature responses of biochemical photosynthesis parameters and leaf nitrogen content within a *Pinus densiflora* crown. *Tree Physiol.* **24**, 737–744 (2004).
- Harley, P., Thomas, R., Reynolds, J. & Strain, B. Modelling photosynthesis of cotton grown in elevated CO₂. *Plant Cell Environ.* **15**, 271–282 (1992).
- Onoda, Y., Hikosaka, K. & Hirose, T. The balance between RuBP carboxylation and RuBP regeneration: a mechanism underlying the interspecific variation in acclimation of photosynthesis to seasonal change in temperature. *Funct. Plant Biol.* **32**, 903–910 (2005).
- Walcroft, A., Le Roux, X., Diaz-Espejo, A., Dones, N. & Sinoquet, H. Effects of crown development on leaf irradiance, leaf morphology and photosynthetic capacity in a peach tree. *Tree Physiol.* **22**, 929–938 (2002).
- Wang, K. Y., Kellomäki, S. & Laitinen, K. Acclimation of photosynthetic parameters in Scots pine after three years exposure to elevated temperature and CO₂. *Agr. Forest Meteorol.* **82**, 195–217 (1996).
- Vaz, M. et al. Drought-induced photosynthetic inhibition and autumn recovery in two Mediterranean oak species (*Quercus ilex* and *Quercus suber*). *Tree Physiol.* **30**, 946–956 (2010).
- Zhou, L. et al. Responses of photosynthetic parameters to drought in subtropical forest ecosystem of China. *Sci. Rep.* **5**, 18254 (2015).
- Doughty, C. E. & Goulden, M. L. Seasonal patterns of tropical forest leaf area index and CO₂ exchange. *J. Geophys. Res. Biogeophys.* **113**, G00B06 (2008).
- Wu, J. et al. Partitioning controls on Amazon forest photosynthesis between environmental and biotic factors at hourly to interannual timescales. *Glob. Change Biol.* **23**, 1240–1257 (2017).
- Gunderson, C. A., O'Hara, K. H., Campion, C. M., Walker, A. V. & Edwards, N. T. Thermal plasticity of photosynthesis: the role of acclimation in forest responses to a warming climate. *Glob. Change Biol.* **16**, 2272–2286 (2010).
- Mooney, H. A., Björkman, O. & Collatz, G. J. Photosynthetic acclimation to temperature in the desert shrub, *Larrea divaricata* I. Carbon dioxide exchange characteristics of intact leaves. *Plant Physiol.* **61**, 406–410 (1978).
- Yuan, W. et al. Thermal adaptation of net ecosystem exchange. *Biogeosciences* **8**, 1453–1463 (2011).
- Sage, R. F. & Kubien, D. S. The temperature response of C₃ and C₄ photosynthesis. *Plant Cell Environ.* **30**, 1086–1106 (2007).
- Armond, P. A., Schreiber, U. & Björkman, O. Photosynthetic acclimation to temperature in the desert shrub, *Larrea divaricata*: II. Light-harvesting efficiency and electron transport. *Plant Physiol.* **61**, 411–415 (1978).
- Badger, M., Björkman, O. & Armond, P. An analysis of photosynthetic response and adaptation to temperature in higher plants: temperature acclimation in the desert evergreen *Nerium oleander* L. *Plant Cell Environ.* **5**, 85–99 (1982).
- Atkin, O., Scheurwater, I. & Pons, T. High thermal acclimation potential of both photosynthesis and respiration in two lowland Plantago species in contrast to an alpine congeneric. *Glob. Change Biol.* **12**, 500–515 (2006).
- Doughty, C. E. An in situ leaf and branch warming experiment in the Amazon. *Biotropica* **43**, 658–665 (2011).
- Koch, G. W., Amthor, J. S. & Goulden, M. L. Diurnal patterns of leaf photosynthesis, conductance and water potential at the top of a lowland rain forest canopy in Cameroon: measurements from the Radeau des Cimes. *Tree Physiol.* **14**, 347–360 (1994).
- Tribuzy, E. S. Variações da temperatura foliar do dossel eo seu efeito na taxa assimilatória de CO₂ na Amazônia Central. PhD thesis, Univ. de São Paulo (2005).
- White, A., Cannell, M. G. & Friend, A. D. CO₂ stabilization, climate change and the terrestrial carbon sink. *Glob. Change Biol.* **6**, 817–833 (2000).
- IPCC *Climate Change 2013: The Physical Science Basis* (eds Stocker, T. F. et al.) (Cambridge Univ. Press, 2013).
- Xu, L. et al. Temperature and vegetation seasonality diminishment over northern lands. *Nat. Clim. Change* **3**, 581 (2013).
- Sendall, K. M. et al. Acclimation of photosynthetic temperature optima of temperate and boreal tree species in response to experimental forest warming. *Glob. Change Biol.* **21**, 1342–1357 (2015).
- Likens, G. E. *Long-Term Studies in Ecology* (Springer, New York, 1989).
- Jung, M. et al. Global patterns of land-atmosphere fluxes of carbon dioxide, latent heat, and sensible heat derived from eddy covariance, satellite, and meteorological observations. *J. Geophys. Res. Biogeophys.* **116**, G00J07 (2011).
- Lester, R. E., Close, P. G., Barton, J. L., Pope, A. J. & Brown, S. C. Predicting the likely response of data-poor ecosystems to climate change using space-for-time substitution across domains. *Glob. Change Biol.* **20**, 3471–3481 (2014).
- Cavaleri, M. A., Reed, S. C., Smith, W. K. & Wood, T. E. Urgent need for warming experiments in tropical forests. *Glob. Change Biol.* **21**, 2111–2121 (2015).
- Papale, D. et al. Towards a standardized processing of Net Ecosystem Exchange measured with eddy covariance technique: algorithms and uncertainty estimation. *Biogeosciences* **3**, 571–583 (2006).
- Myneni, R. B., Ramakrishna, R., Nemani, R. & Running, S. W. Estimation of global leaf area index and absorbed PAR using radiative transfer models. *IEEE Trans. Geosci. Remote Sens.* **35**, 1380–1393 (1997).
- Maisongrand, P., Duchemin, B. & Dedieu, G. VEGETATION/SPOT: an operational mission for the Earth monitoring; presentation of new standard products. *Int. J. Remote Sens.* **25**, 9–14 (2004).

56. Vermote, E. F., El Saleous, N. Z. & Justice, C. O. Atmospheric correction of MODIS data in the visible to middle infrared: first results. *Remote Sens. Environ.* **83**, 97–111 (2002).
57. Rahman, A. F., Sims, D. A., Cordova, V. D. & El-Masri, B. Z. Potential of MODIS EVI and surface temperature for directly estimating per-pixel ecosystem C fluxes. *Geophys. Res. Lett.* **32**, 156–171 (2005).
58. Frankenberg, C. et al. New global observations of the terrestrial carbon cycle from GOSAT: patterns of plant fluorescence with gross primary productivity. *Geophys. Res. Lett.* **38**, 351–365 (2011).
59. Lee, J. E. et al. Forest productivity and water stress in Amazonia: observations from GOSAT chlorophyll fluorescence. *Proc. Roy. Soc. B* **280**, 176–188 (2013).
60. Kottek, M., Grieser, J., Beck, C., Rudolf, B. & Rubel, F. World map of the Köppen–Geiger climate classification updated. *Meteorologische Z.* **15**, 259–263 (2006).
61. Qin, J., Yang, K., Liang, S. & Guo, X. The altitudinal dependence of recent rapid warming over the Tibetan Plateau. *Climatic Change* **97**, 321–327 (2009).
62. Liu, D. et al. Contrasting responses of grassland water and carbon exchanges to climate change between Tibetan Plateau and Inner Mongolia. *Agr. Forest Meteorol.* **249**, 163–175 (2018).
63. Wan, Z. & Dozier, J. A generalized split-window algorithm for retrieving land-surface temperature from space. *IEEE Trans. Geosci. Remote Sens.* **34**, 892–905 (1996).
64. Zhu, Z. et al. Greening of the Earth and its drivers. *Nat. Clim. Change* **6**, 701–795 (2016).
65. Weedon, G. P. et al. The WFDEI meteorological forcing data set: WATCH Forcing Data methodology applied to ERA-Interim reanalysis data. *Water Resour. Res.* **50**, 7505–7514 (2014).
66. Jones, P. W. First- and second-order conservative remapping schemes for grids in spherical coordinates. *Mon. Weather Rev.* **127**, 2204–2210 (1999).
67. Battaglia, M., Beadle, C. & Loughhead, S. Photosynthetic temperature responses of *Eucalyptus globulus* and *Eucalyptus nitens*. *Tree Physiol.* **16**, 81–89 (1996).
68. Lin, Y. S., Medlyn, B. E. & Ellsworth, D. S. Temperature responses of leaf net photosynthesis: the role of component processes. *Tree Physiol.* **32**, 219–231 (2012).
69. Farquhar, Gv, von Caemmerer, Sv & Berry, J. A biochemical model of photosynthetic CO₂ assimilation in leaves of C₃ species. *Planta* **149**, 78–90 (1980).
70. Baker, N. R. *Photosynthesis and the Environment* (Kluwer Academic Publishers, 2006).
71. Helliker, B. R. & Richter, S. L. Subtropical to boreal convergence of tree-leaf temperatures. *Nature* **454**, 511 (2008).
72. Michaletz, S. T. et al. The energetic and carbon economic origins of leaf thermoregulation. *Nat. Plants* **2**, 16129 (2016).
73. Lian, X. et al. Spatiotemporal variations in the difference between satellite-observed daily maximum land surface temperature and station-based daily maximum near-surface air temperature. *J. Geophys. Res. Atmos.* **122**, 2254–2268 (2017).

Acknowledgements

This study was supported by the Strategic Priority Research Program (A) of the Chinese Academy of Sciences (Grant No. XDA20050101), the National Natural Science Foundation of China (41530528) and the National Key R&D Program of China (2017YFA0604702). This work used eddy covariance data acquired by the FLUXNET community and in particular by the following networks: AmeriFlux (US Department of Energy, Biological and Environmental Research, Terrestrial Carbon Program (DE-FG02-04ER63917 and DE-FG02-04ER63911)), AfriFlux, AsiaFlux, CarboAfrica, CarboEuropeIP, CarboItaly, CarboMont, ChinaFlux, Fluxnet-Canada (supported by CFCAS, NSERC, BIOCAP, Environment Canada and NRCAN), GreenGrass, KoFlux, LBA, NECC, OzFlux, TCOS-Siberia and USCCC. We acknowledge the financial support to the eddy covariance data harmonization provided by CarboEuropeIP, FAO-GTOS-CO, iLEAPS, Max Planck Institute for Biogeochemistry, National Science Foundation, University of Tuscia, Université Laval and Environment Canada, and the US Department of Energy and the database development and technical support from Berkeley Water Center, Lawrence Berkeley National Laboratory, Microsoft Research eScience, Oak Ridge National Laboratory, University of California-Berkeley and University of Virginia. P.C., J.P. and I.A.J. would like to acknowledge the financial support from the European Research Council Synergy Grant No. ERC-SyG-2013-610028 IMBALANCE-P. P.C. was also supported by the French Agence Nationale de la Recherche Convergence Lab Changement climatique et usage des terres (CLAND). I.A.J. acknowledges the Methusalem funding of the Flemish Community through the Research Council of the University of Antwerp. T.F.K. was supported by the NASA Terrestrial Ecology Program IDS Award NNN17AE86I. J.M. and X.S. are supported by the Terrestrial Ecosystem Science Scientific Focus Area project funded through the Terrestrial Ecosystem Science Program in the Climate and Environmental Sciences Division of the Biological and Environmental Research Program in the US Department of Energy Office of Science. Oak Ridge National Laboratory is supported by the Office of Science of the US Department of Energy under Contract No. DE-AC05-00OR22725. M.C. was supported by a grant overseen by the French National Research Agency (ANR) as part of the Investissements d'Avenir program (ANR-11-LABX-0002-01, Lab of Excellence ARBRE).

Author contributions

S. Piao designed the research. M. H. performed the analysis. S. Piao drafted the paper. All authors contributed to the interpretation of the results and the text.

Competing interests

The authors declare no competing interests.

Additional information

Supplementary information is available for this paper at <https://doi.org/10.1038/s41559-019-0838-x>.

Reprints and permissions information is available at www.nature.com/reprints.

Correspondence and requests for materials should be addressed to S.P.

Publisher's note: Springer Nature remains neutral with regard to jurisdictional claims in published maps and institutional affiliations.

© The Author(s), under exclusive licence to Springer Nature Limited 2019

Reporting Summary

Nature Research wishes to improve the reproducibility of the work that we publish. This form provides structure for consistency and transparency in reporting. For further information on Nature Research policies, see [Authors & Referees](#) and the [Editorial Policy Checklist](#).

Statistical parameters

When statistical analyses are reported, confirm that the following items are present in the relevant location (e.g. figure legend, table legend, main text, or Methods section).

n/a Confirmed

- The exact sample size (n) for each experimental group/condition, given as a discrete number and unit of measurement
- An indication of whether measurements were taken from distinct samples or whether the same sample was measured repeatedly
- The statistical test(s) used AND whether they are one- or two-sided
Only common tests should be described solely by name; describe more complex techniques in the Methods section.
- A description of all covariates tested
- A description of any assumptions or corrections, such as tests of normality and adjustment for multiple comparisons
- A full description of the statistics including central tendency (e.g. means) or other basic estimates (e.g. regression coefficient) AND variation (e.g. standard deviation) or associated estimates of uncertainty (e.g. confidence intervals)
- For null hypothesis testing, the test statistic (e.g. F , t , r) with confidence intervals, effect sizes, degrees of freedom and P value noted
Give P values as exact values whenever suitable.
- For Bayesian analysis, information on the choice of priors and Markov chain Monte Carlo settings
- For hierarchical and complex designs, identification of the appropriate level for tests and full reporting of outcomes
- Estimates of effect sizes (e.g. Cohen's d , Pearson's r), indicating how they were calculated
- Clearly defined error bars
State explicitly what error bars represent (e.g. SD, SE, CI)

Our web collection on [statistics for biologists](#) may be useful.

Software and code

Policy information about [availability of computer code](#)

Data collection

No software was used to collect data.

Data analysis

The analyses and mapping were both performed using MATLAB (R2017b). Details were reported in Analysis section of the Method.

For manuscripts utilizing custom algorithms or software that are central to the research but not yet described in published literature, software must be made available to editors/reviewers upon request. We strongly encourage code deposition in a community repository (e.g. GitHub). See the Nature Research [guidelines for submitting code & software](#) for further information.

Data

Policy information about [availability of data](#)

All manuscripts must include a [data availability statement](#). This statement should provide the following information, where applicable:

- Accession codes, unique identifiers, or web links for publicly available datasets
- A list of figures that have associated raw data
- A description of any restrictions on data availability

All data is available in the main text or the supplementary information. All computer codes used in this study can be provided by the corresponding author upon reasonable requests.

Field-specific reporting

Please select the best fit for your research. If you are not sure, read the appropriate sections before making your selection.

Life sciences Behavioural & social sciences Ecological, evolutionary & environmental sciences

For a reference copy of the document with all sections, see [nature.com/authors/policies/ReportingSummary-flat.pdf](https://www.nature.com/authors/policies/ReportingSummary-flat.pdf)

Ecological, evolutionary & environmental sciences study design

All studies must disclose on these points even when the disclosure is negative.

Study description	<input type="text" value="We provide empirical evidence for the existence of the optimum air temperature of ecosystem-level gross primary productivity, using measurements of in-situ eddy covariance and satellite-derived proxies, and report its global distribution."/>
Research sample	<input type="text" value="The half-hourly eddy-covariance Gross Primary Productivity data were obtained from FLUXNET datasets. A total of 153 individual FLUXNET sites with 663 site-years of GPP data were used in this study. We also used an ensemble of global remote sensing observations. Details can be seen in the Methods section."/>
Sampling strategy	<input type="text" value="N/A"/>
Data collection	<input type="text" value="N/A"/>
Timing and spatial scale	<input type="text" value="N/A"/>
Data exclusions	<input type="text" value="N/A"/>
Reproducibility	<input type="text" value="N/A"/>
Randomization	<input type="text" value="N/A"/>
Blinding	<input type="text" value="N/A"/>
Did the study involve field work?	<input type="checkbox"/> Yes <input checked="" type="checkbox"/> No

Reporting for specific materials, systems and methods

Materials & experimental systems

- | | |
|-------------------------------------|--|
| n/a | Involvement in the study |
| <input checked="" type="checkbox"/> | <input type="checkbox"/> Unique biological materials |
| <input checked="" type="checkbox"/> | <input type="checkbox"/> Antibodies |
| <input checked="" type="checkbox"/> | <input type="checkbox"/> Eukaryotic cell lines |
| <input checked="" type="checkbox"/> | <input type="checkbox"/> Palaeontology |
| <input checked="" type="checkbox"/> | <input type="checkbox"/> Animals and other organisms |
| <input checked="" type="checkbox"/> | <input type="checkbox"/> Human research participants |

Methods

- | | |
|-------------------------------------|---|
| n/a | Involvement in the study |
| <input checked="" type="checkbox"/> | <input type="checkbox"/> ChIP-seq |
| <input checked="" type="checkbox"/> | <input type="checkbox"/> Flow cytometry |
| <input checked="" type="checkbox"/> | <input type="checkbox"/> MRI-based neuroimaging |